GEOPHYSICS, VOL. 86, NO. 1 (JANUARY-FEBRUARY 2021); P. T61–T74, 11 FIGS.
10.1190/GEO2020-0324.1

Application of the generalized finite-element method to the acoustic wave simulation in exploration seismology

Edith Sotelo[1], Marco Favino[2], and Richard L. Gibson Jr.[3]

ABSTRACT

The generalized finite-element method (GFEM) has been applied frequently to solve harmonic wave equations, but its use in the simulation of transient wave propagation is still limited. We have applied GFEM for the simulation of the acoustic wave equation in models relevant to exploration seismology. We also perform an assessment of its accuracy and efficiency. The main advantage of GFEM is that it provides an enhanced solution accuracy compared to the standard finite-element method (FEM). This is attained by adding user-defined enrichment functions to standard FEM approximations. For the acoustic wave equation, we consider plane waves oriented in different directions as the enrichments, whose argument includes the largest wavenumber of the wavefield. We combine GFEM with an unconditionally stable time integration scheme with a constant time step. To assess the accuracy and efficiency of GFEM, we compare the GFEM simulation results against those obtained with the spectral-element method (SEM). We use SEM because it is the method of choice for wave propagation simulation due to its proven accuracy and efficiency. In the numerical examples, we first perform a convergence study in space and time, evaluating the accuracy of both methods against a semianalytical solution. Then, we consider simulations of relevant models in exploration seismology that include low-velocity features, an inclusion with a complex geometric boundary and topography. Results using these models indicate that GFEM presents comparable accuracy and efficiency to those based on SEM. For the given examples, the GFEM efficiency stems from the combined effect of local mesh refinement, nonconforming or unstructured, and the unconditionally stable time integration scheme with a constant time step. Moreover, these features provide great flexibility to the GFEM implementations, proving advantageous when using, for example, unstructured grids that impose severe time step size restrictions in SEM.

INTRODUCTION

Numerical simulations of wave propagation play a relevant role in several exploration seismology applications, such as seismic imaging (Baysal et al., 1983; Zhu and Lines, 1998; Cho et al., 2019) and field parameter estimation (Vigh and Starr, 2008; Virieux and Operto, 2009). In these applications, it is common to find geologic structures characterized by complex geometric boundaries and/or large contrasts in the material properties with respect to the surrounding rock. For instance, carbonate reservoirs present near-surface diagenetic features that are a product of massive dissolution, collapse, and fracturing of rocks (Wright and Smart, 1994; Lucia, 1999), which result in the formation of caves, vugs, and fracture systems with irregular geometries (Lindsay et al., 2006; Huang et al., 2017). High impedance contrast can be found at the interfaces between an intact rock and collapsed structures partially filled with different material such as loose sediments, breccias, or water (Lucia, 1999; Regone et al., 2017). Furthermore, discontinuous material properties and rough interfaces reduce the smoothness of the solution of the underlying partial differential equation, i.e., the solution presents a reduced differentiability. These geologic characteristics

Manuscript received by the Editor 17 May 2020; revised manuscript received 21 August 2020; published ahead of production 13 October 2020; published online 22 January 2021.
[1]Formerly Texas A&M University, Department of Geology & Geophysics, College Station, Texas 77845-3115, USA; presently University of Lausanne, Institute of Earth Sciences, Geopolis Building, UNIL-Mouline, CH-1015 Lausanne, Switzerland. E-mail: edith.sotelogamboa@unil.ch (corresponding author).
[2]University of Lausanne, Institute of Earth Sciences, Geopolis Building, UNIL-Mouline, CH-1015 Lausanne, Switzerland. E-mail: marco.favino@unil.ch.
[3]Formerly Texas A&M University, Department of Geology & Geophysics, College Station, Texas 77845-3115, USA; presently NanoSeis, LLC, 400 East Arapahoe Road, Suite 305, Centennial, Colorado 80112, USA. E-mail: rick.gibson@nanoseis.com.

pose challenges for the creation of suitable computational meshes and for the choice of suitable simulation methods.

Irregular free surfaces also pose meshing issues as meshes have to conform as close as possible to the irregular boundaries to obtain accurate numerical solutions. Examples of features with irregular surfaces include sand dunes, dry river beds, salt flats, and collapse-filled karst, among others (Bridle et al., 2007; Keho and Kelamis, 2012), which in general cause body and surface wave scattering and may also trap seismic energy producing unwanted multiples (Keho and Kelamis, 2012). Furthermore, free surface conditions create complex wavefields whose simulation requires accurate and cost-effective numerical methods.

The finite-difference method (FDM) has been widely used to simulate wave propagation due to its simplicity of implementation and to the fact that it can be easily coupled with explicit time integration schemes. However, its main disadvantage is the lack of flexibility when domains of complex shapes are considered. Although new approaches aim to address this issue, they require the implementation of special numerical procedures making FDM less attractive. For instance, Appelo and Petersson (2009) incorporate complex geometry on free surfaces by extending the work of Nilsson et al. (2007), who introduce boundary-modified difference operators. Similarly, Lan and Zhang (2011) propose a further extension of the method to three dimensions including anisotropy of the medium. However, as stated by Appelo and Petersson (2009), these implementations are less efficient than standard FDM because they involve more complicated stencils.

In contrast to FDM, the standard finite-element method (FEM) allows flexible meshing without the need of particular implementations, proving to be a versatile numerical method capable of obtaining accurate numerical solutions (Marfurt, 1984) even for complicated geometric boundaries (Frehner et al., 2008; De Basabe and Sen, 2009). However, FEM presents efficiency issues for the simulation of wave propagation, even when combined with explicit time integration schemes because it involves the solution of a large linear system at each time step (Cohen and Fauqueux, 2000). Indeed, low-order polynomial approximations require excessively fine meshes as the wavenumber increases to reduce the dispersion error and obtain numerical solutions with acceptable accuracy (Marfurt, 1984; Ihlenburg and Babuška, 1995b; De Basabe and Sen, 2007). On the other end, although higher order polynomial approximations may provide higher convergence rates for smooth problems (Ihlenburg and Babuška, 1995a; De Basabe and Sen, 2007), the number of degrees of freedom (DOF) could be particularly large.

The spectral-element method (SEM) is one of the first proposed variations of FEM that has a proven capability of improved efficiency for the simulation of wave propagation (Komatitsch and Vilotte, 1998; Komatitsch and Tromp, 1999; Cohen and Fauqueux, 2000). In SEM, the DOF nodes (the basis function nodes) coincide with the quadrature points of a selected quadrature rule. Chebyshev polynomials initially have been proposed as basis functions when SEM was first introduced for solving the wave equation (Priolo et al., 1994; Seriani and Priolo, 1994). Nonetheless, Legendre polynomials, together with a Gauss-Lobatto (GL) quadrature rule, have become the standard for SEM because this formulation yields a mass matrix that is inherently diagonal (Faccioli et al., 1996; Komatitsch and Vilotte, 1998; Cohen and Fauqueux, 2000; Cohen et al., 2001). This property, combined with explicit time integration schemes, allows avoiding the costly solution of a linear system. High-order approximations enable SEM to achieve accurate solutions with low dispersion error (Komatitsch et al., 2005; De Basabe and Sen, 2007) for problems with smooth data and geometries. Nonetheless, high-order approximations impose a strict Courant-Fredrichs-Lewy (CFL) condition, restricting the time step size in simulations, which becomes even more severe when combined with high-order explicit time integration schemes. Moreover, SEM cannot take advantage of the diagonal mass matrix property if combined with nonconforming meshes. Although discontinuous SEM formulations overcome this shortcoming (Käser and Dumbser, 2006; De Basabe et al., 2016), these approaches entail imposing even more severe CFL constraints (De Basabe and Sen, 2010). Nonetheless, the introduction of enrichment functions in these formulations aims to reduce the associated computational cost (Vamaraju et al., 2018).

The generalized FEM (GFEM) is a different strategy to improve the accuracy of FEM. GFEM uses additional basis functions, besides the FEM standard ones, which incorporate user-defined enrichment functions (enrichments) to enhance the approximation of the numerical solution. This avoids the requirement of excessive mesh refinement as the wavenumber increases, without the need of high-order polynomials (Strouboulis et al., 2006, 2008). Typical enrichments are closed-form analytical solutions of particular partial differential equations (Babuška and Sauter, 1997; Strouboulis et al., 2000; Davydov et al., 2017). The enrichments are weighted with standard FEM basis functions, following an approach similar to the partition of unity method (Melenk and Babuška, 1996; Babuška and Melenk, 1997).

Regarding the simulation of wave propagation, GFEM has mostly been applied to solve the harmonic wave equation (i.e., the Helmholtz equation) with a variety of oscillatory enrichments. For instance, Babuška and Sauter (1997) and Strouboulis et al. (2006) propose using plane waves in different directions as additional enrichments and show an improved accuracy of GFEM compared to FEM. Strouboulis et al. (2008) consider other enrichments such as wave band functions and Vekua functions and test the performance and the convergence rate for different meshing strategies. Furthermore, Imbert-Gérard and Monk (2017) propose exponential enrichments (generalized plane waves) with polynomial exponents. They present a discontinuous implementation of the method as well as the corresponding convergence analysis. El Kacimi and Laghrouche (2009) propose a solution for the time-harmonic elastic wave equation incorporating plane waves at different directions to enrich P- and S-waves. They show that it is possible to simulate larger frequencies, without the need of further mesh refinement, while maintaining the accuracy of the solution. Ham and Bathe (2012) expand the application of GFEM to the solution of the transient wave propagation for the acoustic case, but their study is confined to homogeneous media only. In their work, they propose enrichments comprised of multiple harmonic patterns to improve the accuracy of low-order FEM approximations, but they do not evaluate the computational efficiency of this technique. In a similar way, Komijani and Gracie (2017) simulate elastic wave propagation through a fractured media. They use the enrichments proposed by Ham and Bathe (2012) together with specific ones to model discontinuities (Song et al., 2006).

The generalized multiscale FEM (GMsFEM) introduced by Efendiev et al. (2013) is a closely related numerical technique. In this method, additional basis functions are calculated by solving a local problem in a fine mesh, by which local heterogeneities are

captured. Then, they are used to solve numerically the partial differential equation in a coarser mesh. GMsFEM has been applied to simulate acoustic wave propagation (Chung et al., 2014; Chung and Leung, 2016; Fu et al., 2019) and the elastic wave equation (Gao et al., 2015; Cho et al., 2018). In contrast to this method, GFEM introduces user-defined enrichments that are usually part of analytical solutions.

As discussed above, most of the work found in the literature applies GFEM principally to solve harmonic wave equations, either for the acoustic or elastic case, with few applications for the simulation of transient wave propagation. Similarly, accuracy and efficiency assessments of the method for transient wave simulations are still limited. In this work, we extend the GFEM application for the simulaton of the acoustic wave propagation in relevant models for exploration seismology. Furthermore, we perform accuracy and efficiency assessments for the proposed examples. For the GFEM implementation, we follow Strouboulis et al. (2006) and use, as the user-defined enrichments, plane waves in different directions with their wavenumber proportional to the largest wavenumber of the wavefield. Thus, these enrichments mimic radial wave propagation based on a relevant wavenumber. We combine GFEM with an unconditionally stable time integration scheme with a constant time step. This time integration strategy allows, first, the use of time steps that are as coarse as possible, constrained only by a desired level of solution accuracy, and, second, it allows performing the costly matrix factorization for inversion only once, upfront the time loop. Moreover, we use local mesh refinement, unstructured or nonconforming, when needed to reduce the number of DOF. To assess the accuracy and efficiency of GFEM, we compare the GFEM simulation results with those obtained using SEM because this method provides higher accuracy and efficiency than FEM as previously discussed. We implement SEM with a GL quadrature rule that yields a mass diagonal matrix, and we combine it with an explicit time integration scheme because this strategy leads to a trivial solution of the linear system at each time step. In the first numerical example, we perform a convergence study of both methods to assess their accuracy with respect to a semianalytical solution. We also perform an assessment of their efficiency. For the following two examples, we consider more realistic models. For the second case, we present a model with a low-velocity layer and a low-velocity inclusion with a complex geometric boundary. The third case adds a free-surface topography. In these models, we evaluate error estimates and efficiency of GFEM simulations with respect to an SEM reference solution. Overall, the results show that GFEM simulations present similar accuracy and efficiency to those based on SEM. For these examples, the efficiency and utility of GFEM arises from the combined effects of local mesh refinement and the unconditionally stable time integration scheme with constant time step. These same features render GFEM a powerful alternative to SEM.

THEORY AND METHOD

The strong and weak formulations of the acoustic wave equation, as well as the discretization approach, follow the mathematical presentation in Bangerth et al. (2010), which is similar to the treatment of Komatitsch and Vilotte (1998). Moreover, both numerical methods, GFEM and SEM, are implemented in deal.II, an open-source FEM library (Bangerth et al., 2007; Deal.II, 2020).

Acoustic wave equation

Let $\Omega \subset \mathbb{R}^2$ be a bounded domain representing an acoustic medium. The boundary of the domain is denoted by $\partial\Omega$, and its outward normal vector is denoted by $\hat{n}$. The medium has an acoustic velocity c in Ω and a velocity c_b in $\partial\Omega$. We want to find the transient propagation of the pressure p in the time interval $I = (0, T]$ produced by a localized and known source f. The p and f terms are assumed to be functions of the position $\mathbf{x} \in \Omega$ and time $t \in I$. In general, c is assumed to be a function of position $\mathbf{x} \in \Omega$. The mixed formulation of the acoustic wave equation reads (Bangerth et al., 2010)

$$\begin{aligned} \frac{\partial v}{\partial t} &= \nabla \cdot (c^2 \nabla p) + f \quad \text{in } \Omega \times I, \\ \frac{\partial p}{\partial t} &= v \quad \text{in } \Omega \times I, \end{aligned} \tag{1}$$

where v is the time derivative of pressure. Unless stated otherwise, we impose absorbing boundary conditions of the form:

$$\nabla p \cdot \hat{n} = -\frac{1}{c_b}\frac{\partial p}{\partial t} \quad \text{on } \partial\Omega \times I, \tag{2}$$

and zero initial conditions for p and v. The mixed formulation as presented in equation 1 facilitates the use of the θ method for time discretization (Grossmann et al., 2007; Quarteroni and Valli, 2008), which is a straightforward scheme to implement whose stability and convergence have been widely studied.

We define the seismic source as the force density $f = f(\mathbf{x}, t)$, in a way similar to Yue and Guddati (2005):

$$\begin{aligned} f(\mathbf{x}, t) &= a_o f_1(t) f_2(\mathbf{x}), \\ f_1(t) &= f_o (t - t_o) \exp(-\pi^2 f_o^2 (t - t_o)^2) \quad \forall\ t \le 2t_o, \\ f_2(\mathbf{x}) &= \left(1 - \frac{\|\mathbf{x} - \mathbf{x}_o\|^2}{R_s^2}\right)^3 \frac{1}{V} \quad \forall\ \|\mathbf{x} - \mathbf{x}_o\| \le R_s. \end{aligned} \tag{3}$$

Here, a_o is a scaling factor, $f_o = 1/t_o$ is the central frequency of the source, $\mathbf{x}_o$ is the source center, $\|\cdot\|$ is the Euclidean norm, R_s is the source radius, and $V = \pi/4R_s^2$ is the source volume.

Weak formulation

We multiply the first line of equation 1 by a test function $\phi \in V$ and the second line of equation 1 by test function $\psi \in Q$, where V and Q are the two function spaces to be defined later. Applying Gauss' theorem to the divergence term and using the boundary conditions, we express the weak form as

For every $t \in I$, find $p \in V$ and $v \in Q$ such that

$$\begin{aligned} \left(c_b \frac{\partial p}{\partial t}, \phi\right)_{\partial\Omega} + \left(\frac{\partial v}{\partial t}, \phi\right)_{\Omega} &= -(c^2 \nabla p, \nabla \phi)_{\Omega} + (f, \phi)_{\Omega} \quad \forall\ \phi \in V, \\ \left(\frac{\partial p}{\partial t}, \psi\right)_{\Omega} &= (v, \psi)_{\Omega} \quad \forall\ \psi \in Q, \end{aligned} \tag{4}$$

where $(\cdot, \cdot)_{\Omega}$ denotes the L^2 scalar product over the set Ω. Typical choices for the function spaces are $Q = L^2(\Omega)$ and $V = H^1(\Omega)$, where $L^2(\Omega)$ is the space of square-integrable functions over Ω

and $H^1(\Omega)$ is the space of functions with square-integrable derivatives over Ω.

Continuous Galerkin approximations

To discretize equation 4 in space, we introduce a mesh τ covering the domain Ω with quadrilateral elements $\kappa \in \tau$. We introduce a set D of DOF and the basis functions Λ_j with $j \in D$. We define the two approximation spaces as

$$V_h = Q_h := \text{span}\Lambda_j. \tag{5}$$

Hence, the approximations to p and v, respectively, denoted by p_h and v_h, can be expressed as

$$p_h(\mathbf{x}, t) = \sum_{j\in D} P_j(t)\Lambda_j(\mathbf{x}), \qquad v_h(\mathbf{x}, t) = \sum_{j\in D} V_j(t)\Lambda_j(\mathbf{x}). \tag{6}$$

Replacing the definitions of equation 6 in equation 4, we obtain the algebraic formulation

$$\begin{aligned} E\dot{P}(t) + M\dot{V}(t) &= -KP(t) + F(t), \\ M\dot{P}(t) &= MV(t), \end{aligned} \tag{7}$$

where M is the mass matrix, whose components are given by $M_{ij} = (\Lambda_i, \Lambda_j)_\Omega$; K is the stiffness matrix, whose components are given by $K_{ij} = (c^2\nabla\Lambda_i, \nabla\Lambda_j)_\Omega$; and E is the boundary mass matrix, whose components are given by $E_{ij} = (c_b\Lambda_i, \Lambda_j)_{\partial\Omega}$. Moreover, $F(t) = (f(t), \Lambda_i)_\Omega$ is the discretization of the source term.

FEM and basis functions

Standard FEM is based on the polynomial approximation space X_h^σ. In the case of quadrilateral meshes, such a space is defined as

$$X_h^\sigma = \{v \in C^0(\Omega) : v|_\kappa \circ F_\kappa \in \mathbb{Q}_\sigma \quad \forall\, \kappa \in \tau\}, \tag{8}$$

where $F_\kappa : (-1, 1)^2 =: \hat{\kappa} \to \kappa$ is a map from the reference element to the physical element κ and $\mathbb{Q}_\sigma$ is the space of polynomials with degree less than or equal to σ with respect to each of the components of the position vector $\mathbf{x}$. The polynomial basis functions are usually chosen as the Lagrangian nodal functions associated to a node ξ_i, and we denote them by N_i^σ. These basis functions are such that

$$N_i^\sigma(\xi_j) = \delta_{ij}, \tag{9}$$

where δ denotes the Kronecker delta. To specify the dependence of the set of DOF on σ, we denote it by D^σ. For this work, we consider only the space X_h^1 and its piecewise bilinear polynomials N_i as the set of FEM basis functions.

SEM and numerical quadrature

SEM can be treated as a high-order FEM combined with a numerical quadrature rule defined so that the nodes coincide with GL quadrature points. For the polynomial space X_h^σ, we use a GL quadrature rule with $(\sigma + 1)^2$ quadrature points corresponding to the polynomial nodes ξ_i. In this way, the number of quadrature points is the same as the number of nodes for the polynomial space X_h^σ. For the polynomial approximation, we use Lagrangian nodal basis functions N_i^σ with $\sigma \geq 3$.

For instance, the entries of the mass matrix in equation 7 are approximated by the following numerical quadrature:

$$M_{ij} = \int_\Omega N_i^\sigma N_j^\sigma \mathrm{d}x \approx \sum_{k\in D^\sigma} p_k N_i^\sigma(\xi_k) N_j^\sigma(\xi_k), \tag{10}$$

where p_k is the GL quadrature weights. Similar expressions apply for other matrices in equation 7. Because Lagrangian basis functions satisfy the property in equation 9, the GL quadrature rule leads to diagonal matrices M and E. The GL rule is exact for calculating the entries of K if F_κ is linear.

GFEM and enrichment functions

This approximation technique exploits the partition of unity property of the standard FEM basis functions (Babuška and Melenk, 1997), for which $\sum_i N_i^\sigma(\mathbf{x}) = 1$ at any point $\mathbf{x}$. A generalized finite-element function, e.g., p_h, is written as

$$p_h = \sum_{i\in D^{\sigma_1}} P_i N_i^{\sigma_1} + \sum_{l\in D^{\sigma_2}} N_l^{\sigma_2} \sum_{j=1}^{q} P_{l,j} w_q^j, \tag{11}$$

where w_q^j is some global enrichment functions and q is their cardinality.

Following Strouboulis et al. (2006), we choose the space of global enrichment functions as

$$W_q = \text{span}\{w_q^j(\mathbf{x}) = \cos(\mathbf{k}\cdot\mathbf{x})\}, \tag{12}$$

where $\mathbf{k} = k(\cos(2\pi j/q), \sin(2\pi j/q))$, with $j = 0, \ldots, q-1$, are the possible wave vectors for a given wavenumber k. Here, q represents the total number of directions considered. The enrichment function $w_q^j(\mathbf{x}) = \Re[\exp(i\mathbf{k}\cdot\mathbf{x})]$ is the real part of a general plane wave in space traveling in the direction $(\cos(2\pi j/q), \sin(2\pi j/q))$.

With these definitions, we observe from equation 11 that an approximated solution of GFEM can be written as the sum of the parts, one that belongs to the standard finite-element space $X_h^{\sigma_1}$ and one that belongs to the enrichment space:

$$W_q^{\sigma_2} = \text{span}\{N_l^{\sigma_2}(\mathbf{x}) w_q^j(\mathbf{x})\}. \tag{13}$$

Hence, the discretization spaces are defined as $V_h = Q_h = X_h^{\sigma_1} \cup W_q^{\sigma_2}$ and the set of basis functions is $\{N_i^{\sigma_1}\} \cap \{N_l^{\sigma_2} w_q^j\}$. In this work, we consider the case $\sigma_1 = \sigma_2 = 1$. We use a reference wavenumber $k = 2\pi f_o/c_{\min}$ for the enrichments, where f_o is the source reference frequency and $c_{\min}$ is the lowest velocity over the medium. The assembly of matrices and vectors is performed per element as for SEM, and we use Gauss-Legendre quadrature rule to calculate the integrals. To solve the system, we use the frontal solver UMFPACK, which implements the lower-upper (LU) factorization technique for a sparse matrix inversion (Davis and Duff, 1997).

Time integration

Two different θ methods are applied for the time integration in equation 7. We subdivide the time interval $I = (0, T]$ into subintervals

$I_n = (t_{n-1}, t_n)$ of equal length $\Delta t = t_n - t_{n-1}$. Hence, the time-discrete form of equation 7 becomes

$$\frac{E}{\Delta t}[P^n - P^{n-1}] + \frac{M}{\Delta t}[B^n - B^{n-1}] = -K[\theta_1 P^n + (1-\theta_1)P^{n-1}] + [\theta_1 F^n + (1-\theta_1)F^{n-1}],$$
$$\frac{M}{\Delta t}[P^n - P^{n-1}] = M[\theta_2 B^n + (1-\theta_2)B^{n-1}]. \tag{14}$$

For GFEM, we set $\theta_1 = \theta_2 = 0.5$, leading to the Crank-Nicolson or Newmark scheme, which is unconditionally stable (Grossmann et al., 2007). For SEM, we set $\theta_1 = 0$ and $\theta_2 = 1$, obtaining the central difference explicit method for pressure. We use the CFL (Courant et al., 1967) condition to establish the maximum time step size that could be used in the numerical examples. In particular, we check that Δt satisfies the CFL condition, i.e., $\Delta t \leq h_{\min}/c_{\max}$, where $h_{\min}$ is the smallest grid size of the mesh and $c_{\max}$ is the maximum velocity of the medium. However, for SEM, the CFL condition is stricter due to the implementation of high-order polynomials and the presence of unstructured grids (Komatitsch et al., 2005; Quarteroni and Valli, 2008). For GFEM, we restrain the time step to increase the accuracy of the solution.

Nonconforming mesh refinement

We use conforming quadrilateral meshes; however, when needed, we apply local mesh refinement by subdividing each element of a targeted subdomain into four identical elements. This operation leads to nonconforming meshes with hanging nodes, meaning that some vertices of the refined elements will lie on the edge of neighboring unrefined elements (Šolín et al., 2008). This refinement technique produces solutions that are not continuous along the edges with hanging nodes. The continuity of the numerical solution is imposed according to the dominant shape functions, which are the ones corresponding to the coarser elements across an edge with hanging nodes. Thus, we constrain the DOF of the refined elements by a set of linear relationships relating the constrained DOF Dn_i with the unconstrained DOF D_j (Bangerth and Kayser-Herold, 2009):

$$Dn_i = \sum_{j \in I_m} \alpha_{ij} D_j \quad \forall\, i \in I_n, \tag{15}$$

where I_n is the subset of constrained DOF, I_m is the subset of unconstrained DOF, and α_{ij} are the weighting factors relating the ith constrained DOF with the jth unconstrained DOF. In this way, the hanging nodes are not actual DOF.

NUMERICAL EXAMPLES

In this section, we compare GFEM and SEM in terms of accuracy and computational cost by means of three numerical examples. For GFEM simulations, we consider plane waves with three, five, and seven directions. For SEM simulations, we consider polynomial orders three and five. For all of the examples, we define a reference mesh size $h^r = 1.5625$ m and a reference time step size $\Delta t^r = 10^{-4}$ s. We point out that the value h^r is exact for the first numerical example, whereas we tried to create meshes that respect this condition for the second and third numerical examples. We identify the different methods by $s = \text{m}d\text{-}\alpha h\text{-}\beta t$, where m denotes the method (p for SEM and q for GFEM), d denotes either the polynomial order for SEM or the number of plane waves for GFEM, and αh and βt denote the multiples of the reference mesh size and time step size, respectively. For example, $s = \text{q5-}4h\text{-}2t$ denotes a GFEM simulation performed with five enrichment functions, a mesh with mesh size of $4h^r$, and a time step size of $2\Delta t^r$. Note that, for naming the methods, we are simplifying the notation of the mesh and time step size. We are using h instead of h^r and t instead of Δt^r, respectively.

To evaluate the error over space, we define a set of receiver positions $\mathbf{x}_i$ indexed by i and we compute the error as the maximum of the L^2 error over the set of all receivers

$$\text{err}^s = \max_i \|S^s_{\mathbf{x}_i} - S^r_{\mathbf{x}_i}\|_{L^2(I)} = \max_i \left(\int_0^T (S^s_{\mathbf{x}_i} - S^r_{\mathbf{x}_i})^2 \text{d}t \right)^{\frac{1}{2}}, \tag{16}$$

where $S^r_{\mathbf{x}_i}$ and $S^s_{\mathbf{x}_i}$ refer to the reference seismogram and a seismogram obtained using a method s, respectively, at a position $\mathbf{x}_i$. Furthermore, a seismogram $S_{\mathbf{x}_i}(\cdot) = p(\mathbf{x}_i, \cdot)$, meaning that it is the time series of computed pressures at position $\mathbf{x}_i$.

To evaluate the computational cost of SEM and GFEM, we consider solutions presenting the least error for each of the methods. For each of them, we compare the DOF per time step and the seismogram error with respect to CPU time.

Homogeneous medium

The objective of this example is to validate the implementation of the GFEM as well as to test its accuracy and computational cost. In a way similar to Komatitsch and Tromp (1999), we compare the results of our numerical simulations against a reference solution produced by the source $f(\mathbf{x}, t)$ described in equation 3. The reference solution $p^r(\mathbf{x}, t)$ is calculated by applying the representation theorem (Aki and Richards, 1980) over $\mathbb{R}^2$:

$$p^r(\mathbf{x}, t) = \int_{-\infty}^{\infty} d\tau \int_{\mathbb{R}^2} f(\zeta, \tau) G(\mathbf{x}, t; \zeta, \tau) d\zeta, \tag{17}$$

where $G(\mathbf{x}, t; \zeta, \tau)$ is the Green's function of the wave equation. That is, its solution at $(\mathbf{x}, t)$ is due to an impulse force at (ζ, τ). In $\mathbb{R}^2$, the Green's function has the following form (Duffy, 2015):

$$G(\mathbf{x}, t; \zeta, \tau) = \frac{1}{2\pi c^2} \frac{H(t - \tau - r/c)}{\sqrt{(t-\tau)^2 - r^2/c^2}}, \tag{18}$$

where c is the medium velocity, $r = \|\mathbf{x} - \zeta\|$, and $H(\cdot)$ is the Heaviside step function. In this example, the reference solution $p^r(\mathbf{x}, t)$ has been computed by evaluating the integral in equation 17 with Mathematica software. For this reason, we refer to it as the semianalytical solution.

For the numerical simulations, we consider a domain $\Omega = (0, 2l) \times (-l, 0)$ with $l = 400$ m. The medium has a homogeneous acoustic velocity of 1800 m/s. For the source function, we set $f_o = 40$Hz, $R_s = 3.125$ m, and $\mathbf{x}_o = (-l/2, l)$, so that it is located at the center of the domain. We obtain seismograms at the following receiver locations:

$$\mathbf{x}_i^d = \mathbf{x}_o + d\left(\cos\left(\frac{\pi i}{4n}\right), \sin\left(\frac{\pi i}{4n}\right)\right) \quad \text{with } i = 0, \ldots n, \tag{19}$$

with $n = 5$. We set $d = 50$ m for the near-offset receivers and $d = 100$ m for the far-offset receivers. To ensure that no reflections reach any of the receivers, we set the simulation time to 0.12 s, which is shorter than the required time (0.167 s) for the onset of the first reflection at the far receivers.

We perform simulations with mesh sizes of $2h^r$, $4h^r$, $8h^r$, and $16h^r$, and time step sizes of Δt^r, $2\Delta t^r$, $4\Delta t^r$, $8\Delta t^r$, and $16\Delta t^r$. For GFEM, we perform local nonconforming mesh refinement around the source position, so that the mesh size at the source location is always h^r. For SEM, we include simulations with an extra time step size of $0.5\Delta t^r$. For SEM simulations, we do not include local nonconforming mesh refinement to keep the mass matrix diagonal but we double the quadrature points for the computation of $F(t)$ (equations 7 and 14).

Figure 1 shows the semianalytical and the numerically computed seismograms, as well as their difference with respect to the reference seismogram evaluated at two near receivers and two far receivers.

Then, we study the convergence properties in space and time for SEM and GFEM. The errors are evaluated using equation 16 for which the reference seismograms have been obtained evaluating the semianalytical solution at the near and far receiver positions. Figure 2 shows errors with respect to the time step size and mesh size for SEM simulations. According to these results, we observe how refinement in space reduces the error, whereas refinement in time has no effect. This suggests that the restriction on the time step given by the CFL condition provides an accurate enough time step size.

The numerical computation of the semianalytical solution, as well as the use of double-precision floating point numbers, may explain the lack of convergence in the seismogram errors for SEM with p5 for the finest mesh $2h^r$ (Figure 2c and 2d).

In a similar way, Figure 3 reports seismogram errors with respect to the time step size and mesh sizes for GFEM simulations. In this case, we observe that, as the mesh gets finer, the error reduction due to temporal refinement has a more pronounced effect (from $16\Delta t^r$ to $4\Delta t^r$). Conversely, mesh refinement for a fixed time step size has less influence on error reduction as the number of enrichment functions increases. This latter effect on the error can be explained by the additional enrichments that favor the spatial convergence because they consider the wavenumber of the propagating wave.

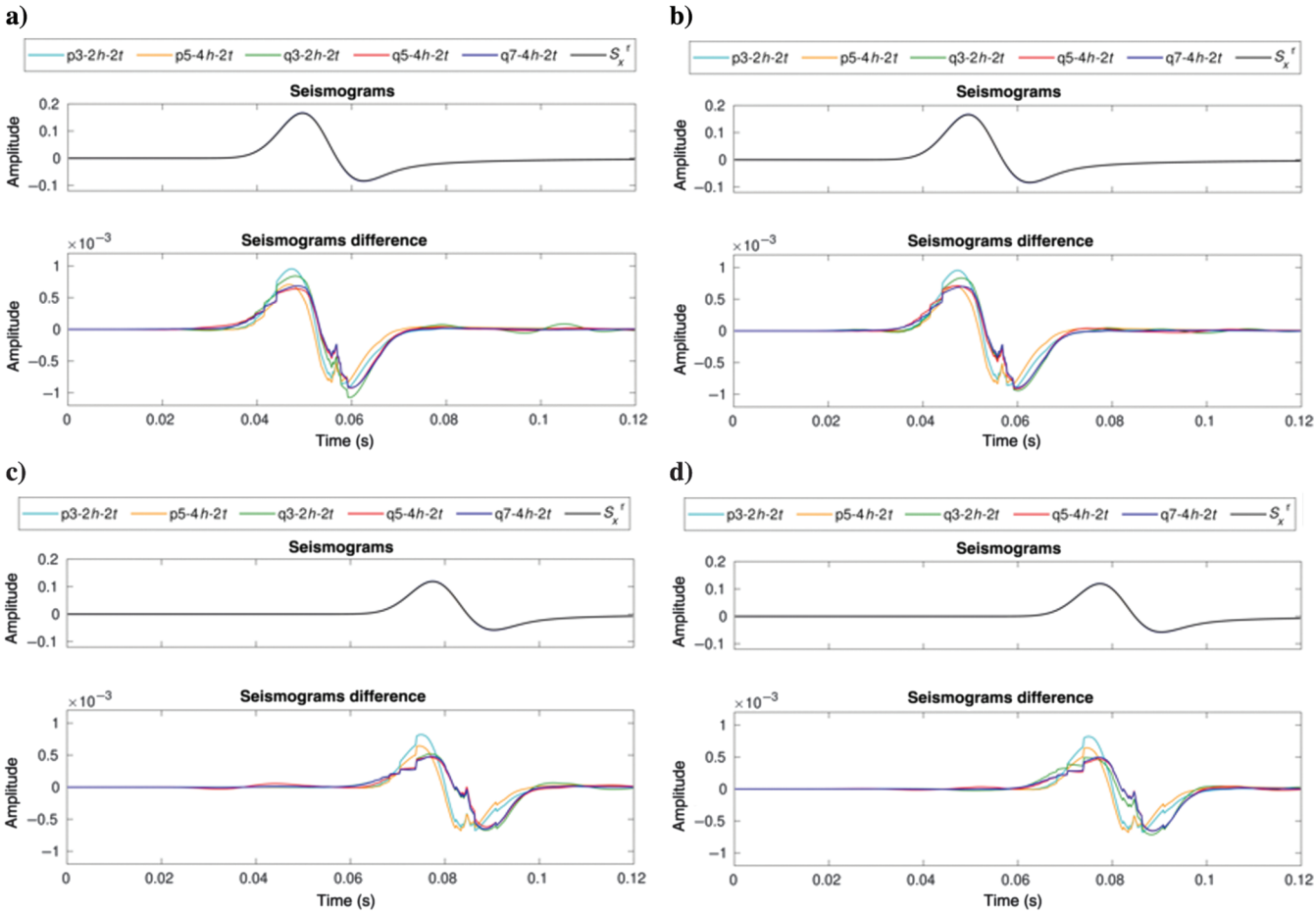

Figure 1. Semianalytical and numerical seismograms, as well as their corresponding difference with respect to the reference seismogram evaluated at two near receivers, (a) 0° and (b) 54°, and two far receivers, (c) 0° and (d) 54°.

Figure 4a reports the CPU time for different computational tasks for both methods as well as their corresponding DOF per time step. The computational tasks that we consider are:

- *Initialization*, which refers to the CPU time spent on the allocation of sparse matrices and vectors according to the sparsity pattern of the mesh. It also considers the CPU time spent in performing nonconforming mesh refinement for GFEM implementations.
- *Assembly*, which corresponds to the CPU time spent on the assembly of the mass, stiffness, and boundary mass matrices.
- *Factorization*, which, for SEM, corresponds to the CPU time spent on finding the reciprocal of the entries in the diagonal of the stiffness matrix and, for GFEM, corresponds to the CPU time spent in computing the LU decomposition of the stiffness matrix that will be used to solve the linear equation at every time step.
- *Time step solve*, which corresponds to the CPU time spent on computing the solution for one time step.

Observe that the first three tasks are performed only once outside of the time advancing scheme. Note as well that, for any example, the major fraction of the CPU time corresponds to the *assembly* time. The *factorization* time is negligible for SEM, but it represents the second largest fraction for GFEM and it increases with the number of plane waves used.

Figure 4b shows the mean seismogram errors between far and near receivers with respect to the total CPU time spent for the complete simulation of 0.12 s. This CPU time comprises the time spent on the solution for all time steps and the additional computational tasks out of the time loop. Note that the maximum and minimum CPU times correspond to GFEM simulations. Nonetheless, the least error belongs to SEM with p5.

Medium with low-velocity features

For this example, we consider a medium with a top low-velocity layer (900 m/s) and a low-velocity inclusion (1500 m/s) as shown in Figure 5a. The model dimensions and the source parameters are the same as in the previous case. For this example, the source is located at (400 m, −50 m) in the horizontal and vertical coordinates, respectively (Figure 5a), and 100 receivers are placed at 10 m from the surface, spanning from 50 to 750 m along a horizontal line.

We consider the solution computed with SEM p5-2h as the reference solution. For this SEM method, a wavelength is sampled by 43.2 DOF nodes. This value is obtained by applying the formula suggested by Komatitsch et al. (2005): $(p+1)c/(f_o 2h)$.

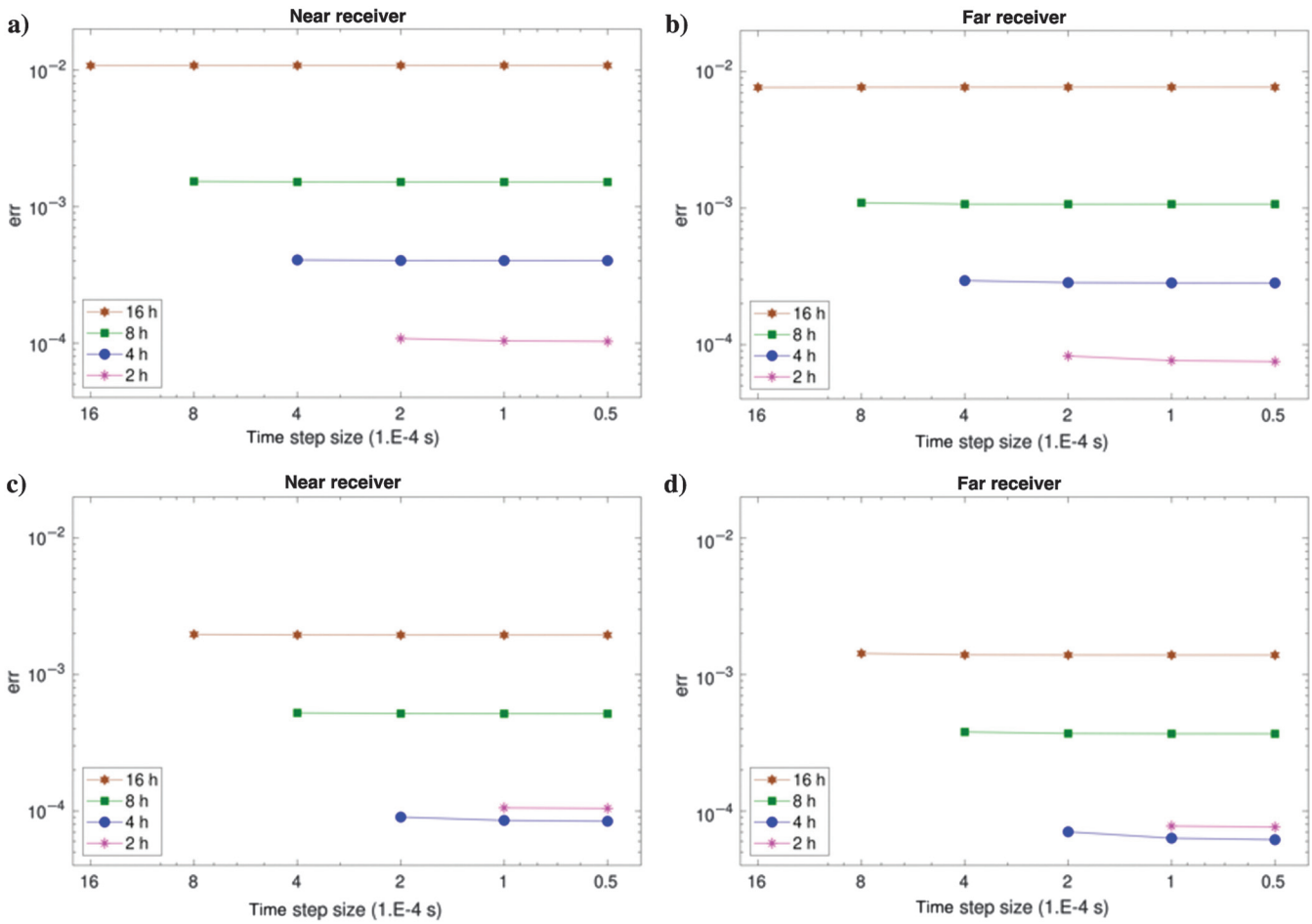

Figure 2. Seismogram errors for the SEM simulations as a function of time step size for different mesh sizes. Results for p3 at (a) near and (b) far receivers. Results for p5 at (c) near and (d) far receivers. Errors calculated using equation 16.

Moreover, this sampling is the same as for the SEM solution in the homogeneous case with p5-4h, which presented the smallest error (order of 10^{-4}). We also compute a second solution with p5-4h. The time step size for these SEM examples is found by decreasing the reference time step Δt^r in a geometric manner: $0.5^n \Delta t^r$, with n belonging to the positive integers, until the solution converges.

For the GFEM cases, we perform simulations with q3, q5, and q7. We set the wavenumber k equal to 0.28m^{-1}, which corresponds to the wavenumber at the top low-layer velocity. Moreover, we apply a local nonconforming mesh refinement at the top low-velocity layer to improve the efficiency of the GFEM simulations. Specifically, we refine the mesh of this layer to $2h^r$, whereas for the rest of

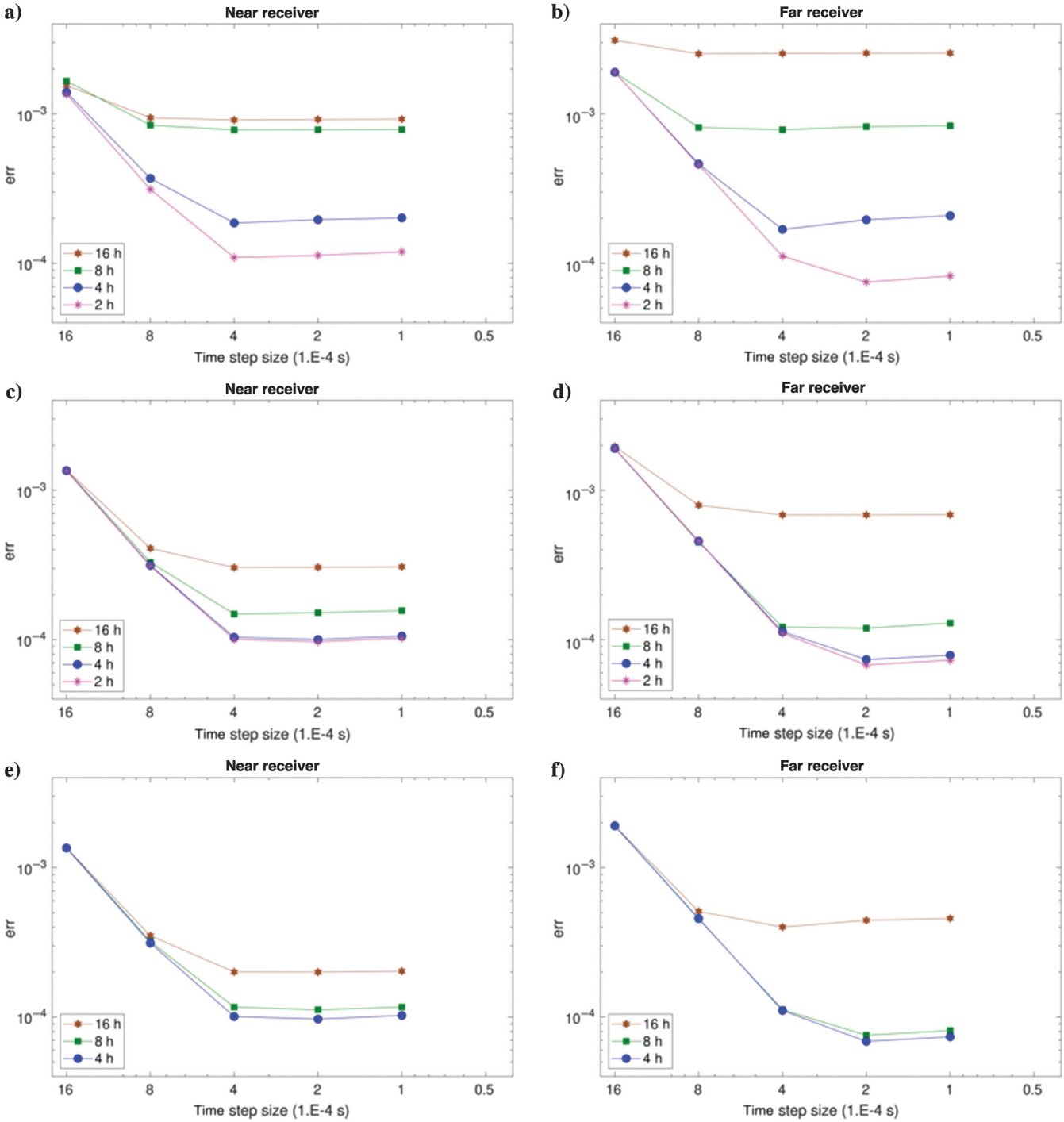

Figure 3. Seismogram errors for the GFEM simulations as a function of the time step size for different mesh sizes. Results for q3 at (a) near and (b) far receivers, for q5 at (c) near and (d) far receivers, and for q7 at (e) near and (f) far receivers. Errors calculated using equation 16.

the domain, the mesh size is kept at $4h^r$. Figure 5b shows an example of a nonconforming mesh that is two times coarser than the one used for the GFEM simulations. For the given mesh size of $2h^r$ at the top low-velocity layer, one wavelength in this layer is sampled by 86.4 DOF nodes and 115.2 DOF nodes for q5 and q7, respectively. Observe that this computation has been obtained by modifying the formula from Komatitsch et al. (2005): $2(q+1)c/(f_o 2h)$. Moreover, note that these samplings correspond to the GFEM solutions in the homogeneous case with the fewest errors (order of 10^{-4}), obtained with q5-4h and q7-4h, respectively. However, to obtain a similar level of accuracy with q3, an additional mesh refinement is required.

Figure 6 reports SEM and GFEM seismograms as well as their difference with respect to the reference seismogram. Notice that differences are of the order of 10^{-4} and for practical terms they overlay each other. Figure 7a reports the number of DOF for SEM and GFEM methods. Figure 7b shows seismogram errors with respect to the total CPU for a simulation time of 0.65 s. The error for each method is calculated following equation 16, meaning that it is the maximum of the L^2 error over the set of the receiver seismograms. Notice that for almost all solutions this error is less than 10^{-4} except for methods q3-4h/2h with $1\Delta t^r$ and $0.5\Delta t^r$. Regarding the CPU time, the two fastest simulations presenting seimogram errors smaller than 10^{-4} correspond to the methods q5-4h/2h-1t and q7-4h/2h-1t.

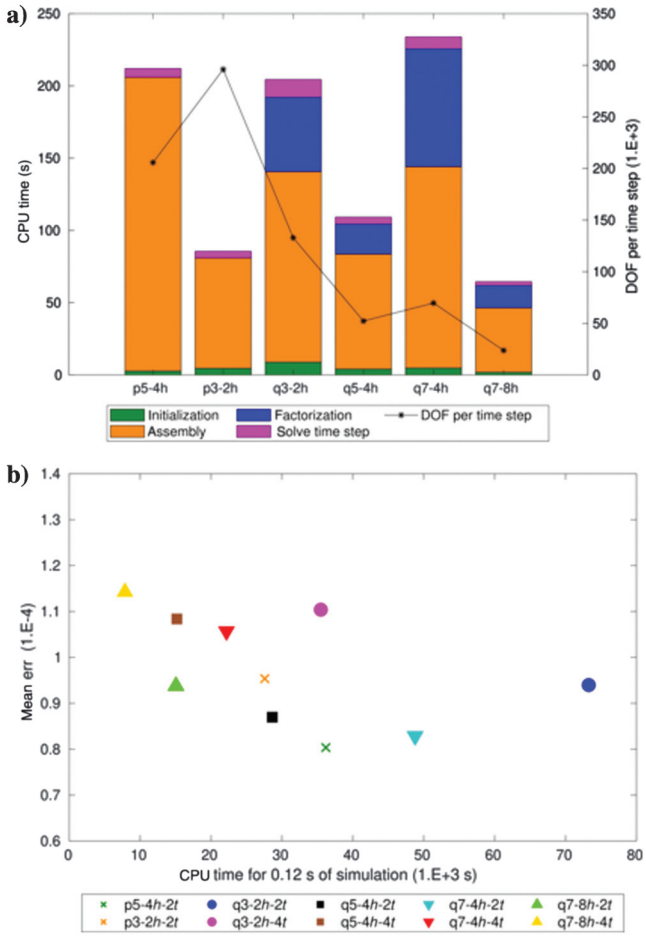

Figure 4. (a) CPU times for different computational tasks and DOF per time step for the best SEM and GFEM solutions. (b) Mean error of the far and near receiver seismograms with respect to CPU time for 0.12 s of simulation.

Model with topography

This model is similar to the previous one except that it presents a topographic relief as shown in Figure 8. The source and receiver locations are the same as in the previous model. The reference solution is computed with SEM p5-2h in a mesh as shown in Figure 9a. For this case, the top layer presents a mesh size of 2 h^r and the rest of the domain presents a mesh size of 4 h^r. At the top low-velocity layer, a wavelength is sampled by 43.2 DOF nodes. Moreover, we use a time step size of 0.25 Δt^r, which is obtained in the same way as in the previous case. We also find an additional SEM solution with p3 and GFEM solutions with q5 and q7 in a mesh that is two times coarser than the mesh used for the reference solution except around the topographic boundary where it has the same size (Figure 9b). This is done to avoid errors that may come from the mismatch with the topographic boundary. Notice that we do not present an additional SEM solution with p5 because we found that it has a stricter CFL condition than for the reference solution. We do not present a GFEM solution with q3 either because the mesh used for the additional solutions is too coarse to obtain results with errors in the order of 10^{-4}. For the SEM solution with p3, one wavelength at the top low-velocity layer is sampled by 28.8 and 14.4 DOF nodes in mesh sizes of 2 h^r and 4 h^r, respectively. For the GFEM examples, one wavelength at the top low-velocity layer is sampled by 86.4 and 43.2 DOF nodes for q5 and by 115.2 and

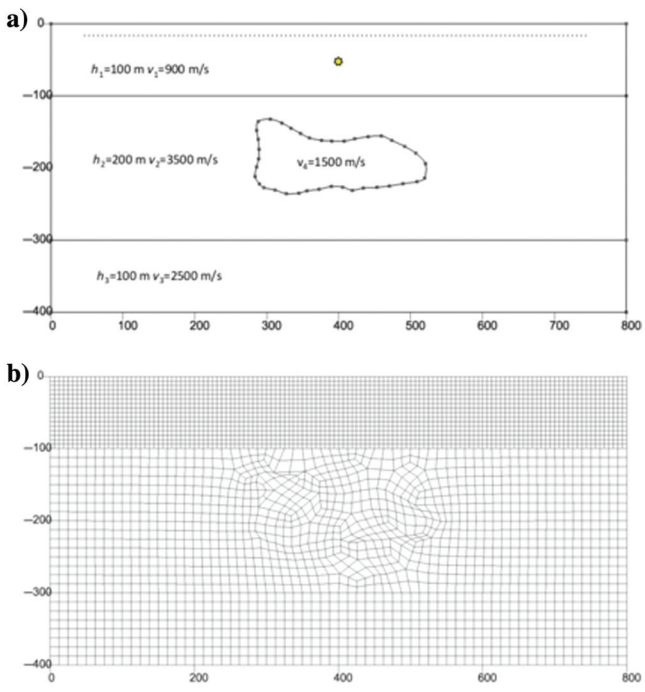

Figure 5. (a) Model with top low-velocity layer and low-velocity inclusion. The source is depicted by a yellow star, and the array of receivers is denoted by a dotted line. (b) Nonconforming mesh example with size 4 h^r for the top low-velocity layer and 8 h^r for the rest of the domain.

57.6 DOF nodes for q7, respectively. Furthermore, the GFEM plane waves include the highest wavenumber of the wavefield (0.28 m^{-1}).

Figure 10 shows the seismograms obtained with SEM and GFEM methods, as well as their difference with respect to the reference seismogram. Figure 11a presents the DOF per time step for SEM and GFEM simulations. Figure 11b shows the seismogram errors with respect to total CPU time for a simulation time of 0.65 s. The error for each method is calculated following equation 16, meaning that it is the maximum of the L^2 error over the set of the receiver seismograms. Notice that, for the GFEM simulation with q7, errors become smaller as the time step size is reduced; a similar behavior is observed for q5, but for this case the smallest time step size (1 Δt^r) does not further reduce the error. GFEM simulations with time step size of $2\Delta t^r$ present errors and CPU times similar to the additional SEM simulation (error = 3.2×10^{-4}; CPU time = 29.8×10^3 s). Specifically, the GFEM simulation with q7 shows a smaller error (2.0×10^{-4}) but slightly higher CPU time (30.9×10^3 s), whereas the GFEM simulation with q5 shows a

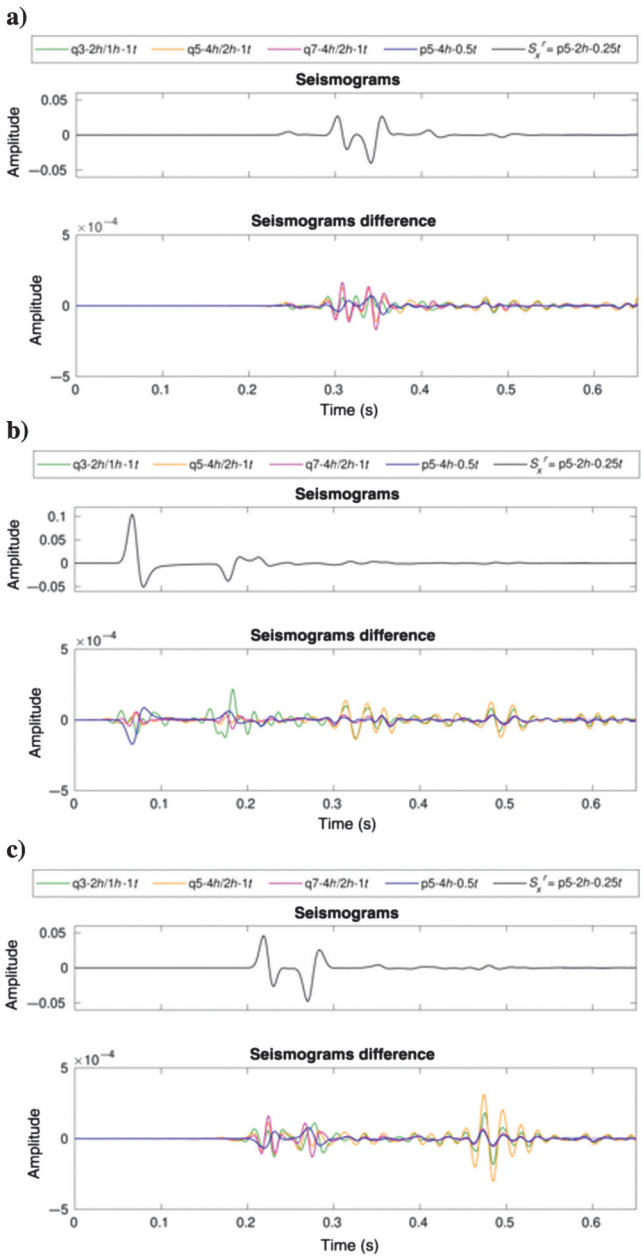

Figure 6. SEM and GFEM seismograms and their difference with respect to the reference seismogram. Evaluations performed for receivers at (a) 156, (b) 403.5, and (c) 580 m in the horizontal coordinates.

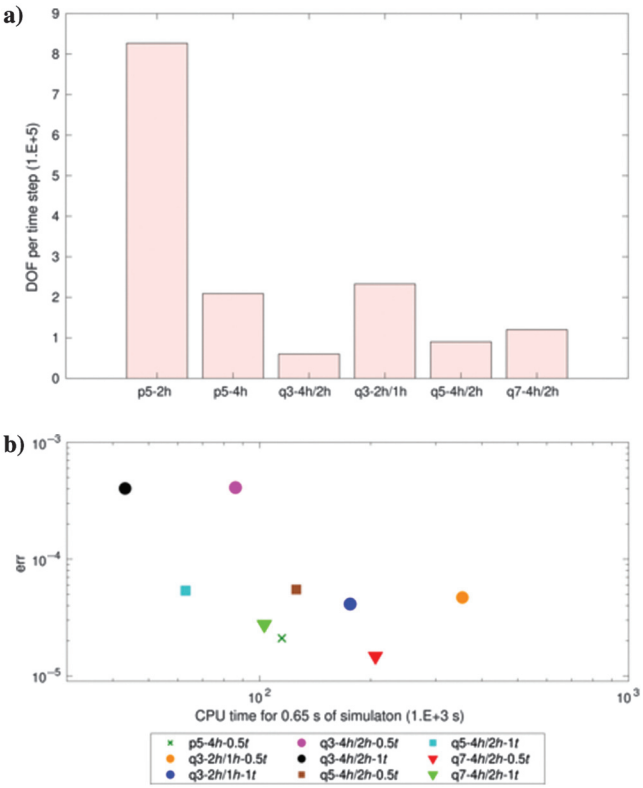

Figure 7. (a) DOF per time step for the SEM and GFEM solutions. (b) Seismogram errors with respect to CPU time for 0.65 s of simulation for the SEM and GFEM examples. Errors calculated using equation 16. The CPU time for the SEM reference solution is 906×10^3 s.

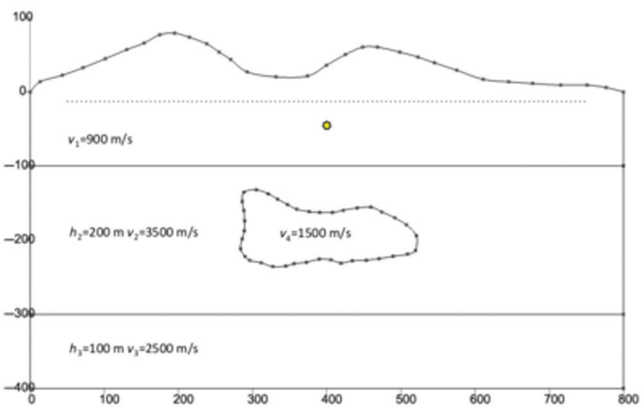

Figure 8. Similar model as in Figure 5 but including topography. The source is depicted by a yellow star, and the array of receivers is denoted by a dotted line.

higher error (4.1×10^{-4}) but with a faster simulation time (21.5×10^3 s). GFEM simulations with a coarser time step size ($4\,\Delta t^r$) have even higher errors (approximately 8.0×10^{-4}), but they present much faster CPU times than the additional SEM solution.

DISCUSSION

We have performed a comparison of accuracy and efficiency between GFEM and SEM for the case of the acoustic wave propagation. We used SEM as the reference method because it is the preferred method for wave simulation due to its high accuracy and efficiency. Nonetheless, numerical results from this work suggest that GFEM can be a flexible alternative to SEM, while providing a comparable accuracy and efficiency. This is particularly true when unstructured fine meshes are needed to conform to complicated boundaries; hence, the exponential convergence of SEM cannot be exploited. Moreover, GFEM may be preferable to SEM when local nonconforming refinement is performed in certain areas of the domain to increase the solution accuracy. In this case, the use of such meshes produces nondiagonal mass matrices, removing the main feature that leads to the choice of SEM.

The first example allowed the evaluation of the convergence properties of GFEM and SEM by comparing the L^2 error of the seismograms. The first interesting observation is that, for SEM, refinements of the temporal grid do not reduce the error (Figure 2). Assuming that, as for other time-dependent equations (Karaa, 2011), the error can be bounded by the sum of spatial and temporal discretization components, this suggests that the spatial component of the error dominates over the temporal one. Hence, the time step size provided by the CFL condition is already optimal. However, the time step size of GFEM is not constrained by the CFL condition. In this case, we observe that refinements of the temporal grid reduce the error (Figure 3), especially when the spatial mesh becomes finer.

GFEM results from the first example provide an initial insight into the appropriate mesh size and number of plane waves needed to attain a certain level of accuracy. According to Figure 4b, the best results in terms of accuracy and CPU cost correspond to GFEM

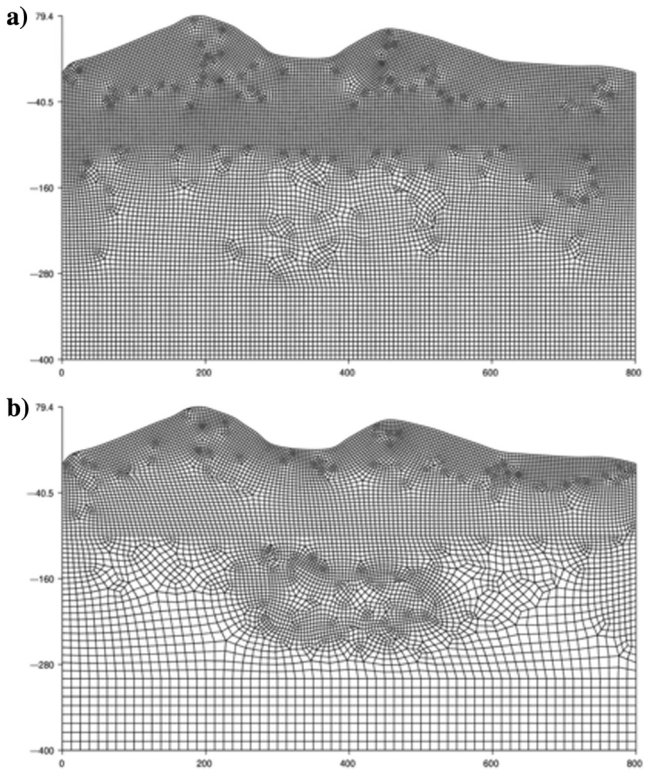

Figure 9. (a) Unstructured mesh used to obtain the SEM reference solution. (b) Mesh two times coarser than the reference mesh except in the areas close to the boundary in which the grid sizes are the same. This mesh is used to find additional SEM and GFEM solutions.

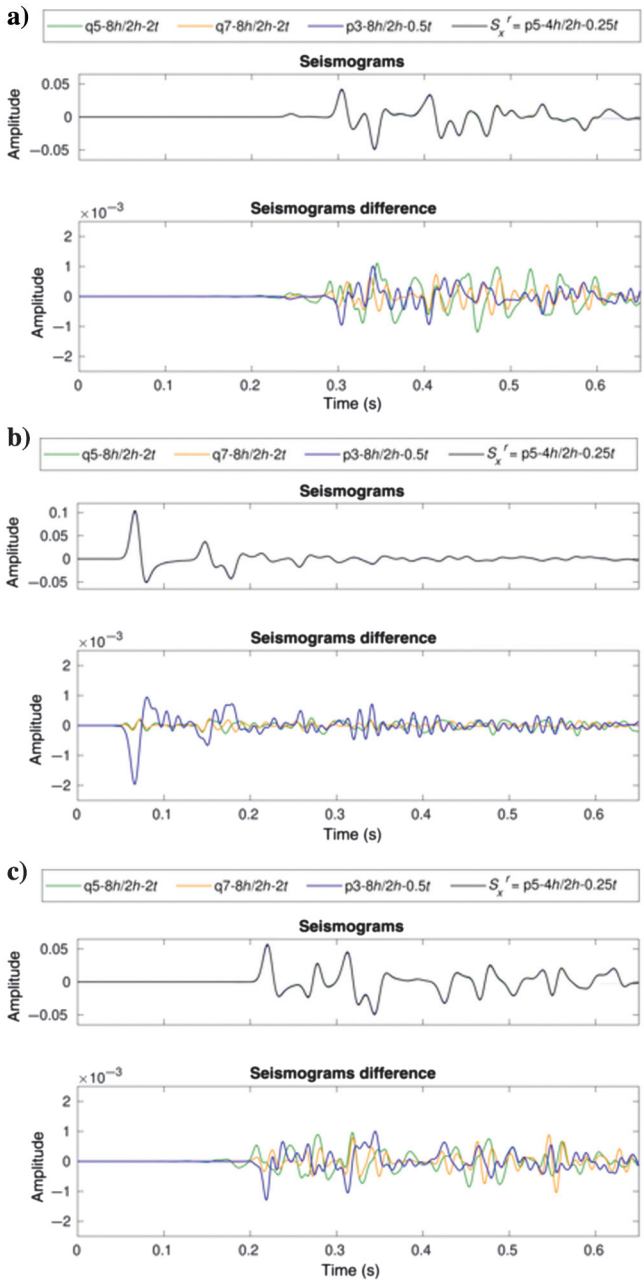

Figure 10. SEM and GFEM seismograms and their difference with respect to the reference seismogram. Evaluations performed for receivers at (a) 156, (b) 403.5, and (c) 580 m in the horizontal coordinates.

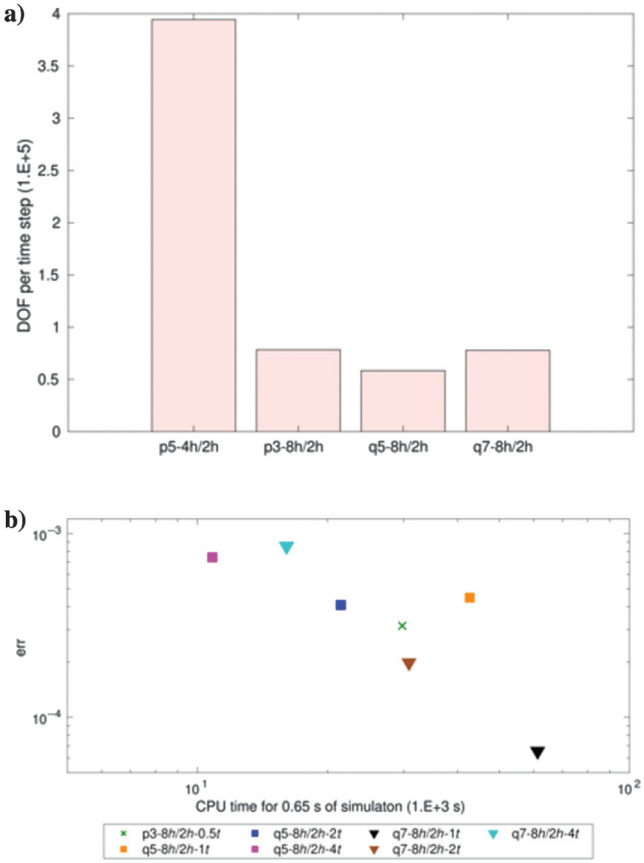

Figure 11. (a) DOF per time step for the SEM and GFEM simulations. (b) Seismogram errors with respect to CPU time for 0.65 s of simulation for the SEM and GFEM examples. Errors calculated using equation 16. The CPU time for the SEM reference solution is 429×10^3s.

solutions with q5-4h-2t, q7-4h-4t, and q7-8h-2t. For these solutions, the DOF nodes per wavelength are 86.4, 115.2, and 57.6, correspondingly, and we used these sampling values as a guideline for the two following examples. Regarding the selection of the time step size, given that for the GFEM simulations we have used nonconforming mesh refinement around the source, with a minimum mesh size of Δh^r, then the maximum time step size permitted by the CFL condition would be $\Delta t_r = 8.7 \times 10^{-4}$ s. If we take this value as a reference, then, for instance, the time step sizes of 2 Δt^r and 4 Δt^r used for the GFEM solutions (Figure 4b) are equivalent to $0.23\Delta t_r$ and $0.46\Delta t_r$, respectively.

The two other examples show meshing techniques that enable GFEM to reach a desired level of accuracy in a cost-effective way. In the second example, we apply a nonconforming mesh refinement in the top low-velocity layer, which allows us to obtain results comparable to SEM in terms of accuracy and efficiency (Figure 7b) without adding excessive cost as in the case of a uniform mesh. In the third example, we use an unstructured mesh, which is fine close to the topographic boundary and coarser on the rest of the medium. In this case, we found that for SEM with p5 the numerical solution diverged for the same time step size used for the reference solution (0.25 Δt^r). This is because mesh distortion makes the CFL condition stricter in SEM implementations (Komatitsch et al., 2005). In contrast, GFEM is not affected by this constraint, providing GFEM with more flexibility in this regard.

GFEM can present comparable efficiency to SEM as a consequence of the combined effect of its speed to solve for a single time step (see, for instance, in Figure 4a, examples q5-4h and q7-8h) and of its flexibility to use larger time step sizes. This is a direct consequence of the use of an unconditionally stable time integration scheme with a constant time step that allows the LU factorization of the system matrix to be performed upfront the time loop. Especially for long simulation times, this feature outweighs the initial costly factorization rendering the method cost effective. However, if nonuniform time steps are used, the efficiency degrades; nevertheless, parallel implementations of the solvers are available (Amestoy et al., 2000). Another important observation is that for the GFEM seismograms presented there is not visible dispersion despite of the use of a low-order polynomial. This is also corroborated by the error estimations presented, which, for specific GFEM simulations, are of the same order as SEM.

GFEM has some shortcomings as well. In this aspect, we note that the quadrature rule used for the assembly of the matrices is not exact because GFEM incorporates sinusoidal functions whose frequencies depend on the wavenumber. As a consequence, higher order quadrature rules would be needed for larger wavenumbers. In our numerical examples, we used a Gauss-Legendre quadrature rule of order four. Nonetheless, for the sake of testing its accuracy, in the first example we also performed simulations with a Gauss-Legendre quadrature rule of order 10 and, when comparing the corresponding results, the differences were on the order of 10^{-7}. Another issue is that stiffness and mass matrices in the global system of equations may be singular due to the linear dependency of the additional basis functions (Strouboulis et al., 2000). In the simulations, we used the frontal direct solver UMFPACK (Davis, 2004) and we did not encounter any problem related to singularity or ill-conditioning of the stiffness matrix. However, if the issue arises for problems with larger DOF, matrix regularization algorithms can be incorporated (Strouboulis et al., 2000; Ham and Bathe, 2012).

CONCLUSION

We have applied GFEM, coupled with a Newmark time integration scheme, for the simulation of the acoustic wave propagation for relevant models in exploration seismology that include low-velocity features, complex geometric boundaries, and a topographic free surface. This approach has been systematically compared with a standard one based on SEM and an explicit second-order time integration scheme, in terms of accuracy and efficiency. Numerical results show that the GFEM-based approach can achieve similar accuracy and efficiency as the SEM-based one. This is particularly true for cases with nonsmooth data and/or domains with complicated boundaries or inclusions, in which the high accuracy of SEM cannot be exploited.

GFEM improves the accuracy of standard FEM by adding enrichment functions. For the presented simulations, GFEM produces numerical solutions that do not have the dispersion error typical of low-order FEM. This is possible because plane-wave enrichment functions mimic the shape of the wavefront together with its wavenumber, thus allowing the use of coarser meshes.

The GFEM implementations can attain an acceptable efficiency because they combine local mesh refinement, nonconforming or unstructured, when needed, together with an unconditionally stable

time integration scheme with constant time step size. In particular, this time integration strategy enables the use of coarser time step sizes than the ones used in SEM. Moreover, the use of a constant time step size greatly reduces the cost of matrix inversion at each time step because it allows the expensive factorization operation to be performed outside of the time loop. These features also render GFEM a flexible alternative to SEM, especially when CFL constraints become severe for SEM simulations.

The proposed approach opens new research avenues in the field of the discretization methods of the acoustic wave equation. An a priori error estimate has to be developed for the presented method and, more generally, for GFEM coupled with different time integration schemes. In particular, it would be interesting to study if the enrichment functions improve the convergence only with respect to the mesh size or also with respect to the time step size. Moreover, detailed investigations have to be performed to understand how the CFL condition is modified for the GFEM. Finally, such an approach has to be extended to 3D cases and to the elastic wave equation.

ACKNOWLEDGMENTS

The source code for the simulations presented in this paper is available at https://github.com/esotelog/GFEM_acoustic. Part of this work was performed using the resources of the Department of Geology and Geophysics and Berg-Hughes Center for Petroleum and Sedimentary Systems at Texas A&M University. This work was also partially supported by grant no. 200020_178946 from the Swiss National Science Foundation (SNSF) and has been completed within the Swiss Competence Center on Energy Research Supply of Electricity, with the support of Innosuisse. M. Favino acknowledges gratefully the support of the SNSF through grant no. PZ00P2_180112.

DATA AND MATERIALS AVAILABILITY

Data associated with this research are available and can be accessed via the following URL: https://github.com/esotelog/GFEM_acoustic.

REFERENCES

Aki, K., and P. G. Richards, 1980, Quantitative seismology, 2nd ed.: University Science Books.

Amestoy, P. R., I. S. Duff, and J. Y. L'Excellent, 2000, Multifrontal parallel distributed symmetric and unsymmetric solvers: Computer Methods in Applied Mechanics and Engineering, **184**, 501–520, doi: 10.1016/S0045-7825(99)00242-X.

Appelo, D., and N. A. Petersson, 2009, A stable finite difference method for the elastic wave equation on complex geometries with free surfaces: Communications in Computational Physics, **5**, 84–107.

Babuška, I., and J. M. Melenk, 1997, The partition of unity method: International Journal for Numerical Methods in Engineering, **40**, 727–758, doi: 10.1002/(SICI)1097-0207(19970228)40:4<727::AID-NME86>3.0.CO;2-N.

Babuška, I. M., and S. A. Sauter, 1997, Is the pollution effect of the FEM avoidable for the Helmholtz equation considering high wave numbers?: SIAM Journal on Numerical Analysis, **34**, 2392–2423, doi: 10.1137/S0036142994269186.

Bangerth, W., M. Geiger, and R. Rannacher, 2010, Adaptive Galerkin finite element methods for the wave equation: Computational Methods in Applied Mathematics, **10**, 3–48, doi: 10.2478/cmam-2010-0001.

Bangerth, W., R. Hartmann, and G. Kanschat, 2007, Deal.II — A general-purpose object-oriented finite element library: ACM Transactions on Mathematical Software, **33**, 24–27, doi: 10.1145/1268776.1268779.

Bangerth, W., and O. Kayser-Herold, 2009, Data structures and requirements for hp finite element software: ACM Transactions on Mathematical Software, **36**, 1–31, doi: 10.1145/1486525.1486529.

Baysal, E., D. D. Kosloff, and J. W. C. Sherwood, 1983, Reverse time migration: Geophysics, **48**, 1514–1524, doi: 10.1190/1.1441434.

Bridle, R., R. Ley, and A. Al-Mustafa, 2007, Near-surface models in Saudi Arabia: Geophysical Prospecting, **55**, 779–792, doi: 10.1111/j.1365-2478.2007.00639.x.

Cho, Y., R. L. Gibson, S. Fu, and Y. Efendiev, 2019, Frequency-domain reverse-time migration with accelerated wave simulation via generalized multiscale finite element: Journal of Applied Geophysics, **160**, 103–120, doi: 10.1016/j.jappgeo.2018.11.005.

Cho, Y., R. L. Gibson, M. Vasilyeva, and Y. Efendiev, 2018, Generalized multiscale finite elements for simulation of elastic-wave propagation in fractured media: Geophysics, **83**, no. 1, WA9–WA20, doi: 10.1190/geo2017-0076.1.

Chung, E. T., Y. Efendiev, and W. T. Leung, 2014, Generalized multiscale finite element methods for wave propagation in heterogeneous media: Multiscale Modeling & Simulation, **12**, 1691–1721, doi: 10.1137/130926675.

Chung, E. T., and W. T. Leung, 2016, Mixed GMsFEM for the simulation of waves in highly heterogeneous media: Journal of Computational and Applied Mathematics, **306**, 69–86, doi: 10.1016/j.cam.2016.04.001.

Cohen, G., and S. Fauqueux, 2000, Mixed finite elements with mass-lumping for the transient wave equation: Journal of Computational Acoustics, **8**, 171–188, doi: 10.1142/S0218396X0000011X.

Cohen, G., P. Joly, J. E. Roberts, and N. Tordjman, 2001, Higher order triangular finite elements with mass lumping for the wave equation: SIAM Journal on Numerical Analysis, **38**, 2047–2078, doi: 10.1137/S0036142997329554.

Courant, R., K. Friedrichs, and H. Lewy, 1967, On the partial difference equations of mathematical physics: IBM Journal of Research and Development, **11**, 215–234, doi: 10.1147/rd.112.0215.

Davis, T. A., 2004, Algorithm 832: UMFPACK, an unsymmetric-pattern multifrontal method: ACM Transactions on Mathematical Software, **30**, 196–199, doi: 10.1145/992200.992206.

Davis, T. A., and I. S. Duff, 1997, An unsymmetric-pattern multifrontal method for sparse LU factorization: Society for Industrial and Applied Mathematics, **18**, 140–158.

Davydov, D., T. Gerasimov, J.-P. Pelteret, and P. Steinmann, 2017, Convergence study of the *h*-adaptive PUM and the *hp*-adaptive FEM applied to eigenvalue problems in quantum mechanics: Advanced Modeling and Simulation in Engineering Sciences, **4**, 7, doi: 10.1186/s40323-017-0093-0.

Deal.II, 2020, Deal.II — An open source finite element library, https://www.dealii.org/, accessed 12 August 2020.

De Basabe, J. D., and M. K. Sen, 2007, Grid dispersion and stability criteria of some common finite-element methods for acoustic and elastic wave equations: Geophysics, **72**, no. 6, T81–T95, doi: 10.1190/1.2785046.

De Basabe, J. D., and M. K. Sen, 2009, New developments in the finite-element method for seismic modeling: The Leading Edge, **28**, 562–567, doi: 10.1190/1.3124931.

De Basabe, J. D., and M. K. Sen, 2010, Stability of the high-order finite elements for acoustic or elastic wave propagation with high-order time stepping: Geophysical Journal International, **181**, 577–590, doi: 10.1111/j.1365-246X.2010.04536.x.

De Basabe, J. D., M. K. Sen, and M. F. Wheeler, 2016, Elastic wave propagation in fractured media using the discontinuous Galerkin method: Geophysics, **81**, no. 4, T163–T174, doi: 10.1190/geo2015-0602.1.

Duffy, D. G., 2015, Green's functions for the wave equation, *in* Green's functions with applications, 2nd ed.: Chapman and Hall, 161–278.

Efendiev, Y., J. Galvis, and T. Y. Hou, 2013, Generalized multiscale finite element methods (GMsFEM): Journal of Computational Physics, **251**, 116–135, doi: 10.1016/j.jcp.2013.04.045.

El Kacimi, A., and O. Laghrouche, 2009, Numerical modelling of elastic wave scattering in frequency domain by the partition of unity finite element method: International Journal for Numerical Methods in Engineering, **77**, 1646–1669, doi: 10.1002/nme.2471.

Faccioli, E., F. Maggio, A. Quarteroni, and A. Taghan, 1996, Spectral-domain decomposition methods for the solution of acoustic and elastic wave equations: Geophysics, **61**, 1160–1174, doi: 10.1190/1.1444036.

Frehner, M., S. M. Schmalholz, E. H. Saenger, and H. Steeb, 2008, Comparison of finite difference and finite element methods for simulating two-dimensional scattering of elastic waves: Physics of the Earth and Planetary Interiors, **171**, 112–121, doi: 10.1016/j.pepi.2008.07.003.

Fu, S., K. Gao, and E. T. Chung, 2019, A high-order multiscale finite-element method for time-domain elastic wave modeling in strongly heterogeneous media: Journal of Applied Geophysics, **170**, 103852, doi: 10.1016/j.jappgeo.2019.103852.

Gao, K., S. Fu, R. L. Gibson, E. T. Chung, and Y. Efendiev, 2015, Generalized multiscale finite-element method (GMsFEM) for elastic wave propagation in heterogeneous, anisotropic media: Journal of Computational Physics, **295**, 161–188, doi: 10.1016/j.jcp.2015.03.068.

Grossmann, C., H.-G. Roos, and M. Stynes, 2007, Finite element methods for unsteady problems, *in* Numerical treatment of partial differential equations: Springer, 317–373.

Ham, S., and K.-J. Bathe, 2012, A finite element method enriched for wave propagation problems: Computers & Structures, **94-95**, 1–12, doi: 10.1016/j.compstruc.2012.01.001.

Huang, S., Y. Zhang, X. Zheng, Q. Zhu, G. Shao, Y. Cao, X. Chen, Z. Yang, and X. Bai, 2017, Types and characteristics of carbonate reservoirs and their implication on hydrocarbon exploration: A case study from the eastern Tarim Basin, NW China: Journal of Natural Gas Geoscience, **2**, 73–79, doi: 10.1016/j.jnggs.2017.02.001.

Ihlenburg, F., and I. Babuška, 1995a, Dispersion analysis and error estimation of Galerkin finite element methods for the Helmholtz equation: International Journal for Numerical Methods in Engineering, **38**, 3745–3774, doi: 10.1002/nme.1620382203.

Ihlenburg, F., and I. Babuška, 1995b, Finite element solution of the Helmholtz equation with high wave number — Part 1: The h-version of the FEM: Computers & Mathematics with Applications, **30**, 9–37, doi: 10.1016/0898-1221(95)00144-N.

Imbert-Gérard, L.-M., and P. Monk, 2017, Numerical simulation of wave propagation in inhomogeneous media using generalized plane waves: ESAIM: Mathematical Modelling and Numerical Analysis, **51**, 1387–1406, doi: 10.1051/m2an/2016067.

Karaa, S., 2011, Error estimates for finite element approximations of a viscous wave equation: Numerical Functional Analysis and Optimization, **32**, 750–767, doi: 10.1080/01630563.2011.580874.

Käser, M., and M. Dumbser, 2006, An arbitrary high-order discontinuous Galerkin method for elastic waves on unstructured meshes — 1: The two-dimensional isotropic case with external source terms: Geophysical Journal International, **166**, 855–877, doi: 10.1111/j.1365-246X.2006.03051.x.

Keho, T. H., and P. G. Kelamis, 2012, Focus on land seismic technology: The near-surface challenge: The Leading Edge, **31**, 62–68, doi: 10.1190/1.3679329.

Komatitsch, D., and J. Tromp, 1999, Introduction to the spectral element method for three-dimensional seismic wave propagation: Geophysical Journal International, **139**, 806–822, doi: 10.1046/j.1365-246x.1999.00967.x.

Komatitsch, D., S. Tsuboi, and J. Tromp, 2005, The spectral-element method in seismology: Geophysical Monograph, **157**, 205–227, doi: 10.1029/157GM13.

Komatitsch, D., and J.-P. Vilotte, 1998, The spectral element method: An efficient tool to simulate the seismic response of 2D and 3D geological structures: Bulletin of the Seismological Society of America, **88**, 368–392.

Komijani, M., and R. Gracie, 2017, An enriched finite element model for wave propagation in fractured media: Finite Elements in Analysis and Design, **125**, 14–23, doi: 10.1016/j.finel.2016.11.001.

Lan, H., and Z. Zhang, 2011, Three-dimensional wave-field simulation in heterogeneous transversely isotropic medium with irregular free surface: Bulletin of the Seismological Society of America, **101**, 1354–1370, doi: 10.1785/0120100194.

Lindsay, R. F., D. L. Cantrell, G. W. Hughes, T. H. Keith, H. W. Mueller, III, and S. Russell, 2006, Ghawar Arab-D reservoir: Widespread porosity in shoaling-upward carbonate cycles, Saudi Arabia, Giant hydrocarbon reservoirs of the world: From rocks to reservoir characterization and modeling: AAPG Special Volumes, 97–137.

Lucia, F. J., 1999, Diagenetic overprinting and rock-fabric distribution: The massive dis-solution, collapse, and fracturing environment, *in* Carbonate reservoir characterization: Springer, 157–176.

Marfurt, K. J., 1984, Accuracy of finite difference and finite element modeling of the scalar and elastic wave equations: Geophysics, **49**, 533–549, doi: 10.1190/1.1441689.

Melenk, J., and I. Babuška, 1996, The partition of unity finite element method: Basic theory and applications: Computer Methods in Applied Mechanics and Engineering, **139**, 289–314, doi: 10.1016/S0045-7825(96)01087-0.

Nilsson, S., N. A. Petersson, B. Sjögreen, and H.-O. Kreiss, 2007, Stable difference approximations for the elastic wave equation in second order formulation: SIAM Journal on Numerical Analysis, **45**, 1902–1936, doi: 10.1137/060663520.

Priolo, E., J. M. Carcione, and G. Seriani, 1994, Numerical simulation of interface waves by highorder spectral modeling techniques: The Journal of the Acoustical Society of America, **95**, 681–693, doi: 10.1121/1.408428.

Quarteroni, A., and A. Valli, 2008, Parabolic problems, Numerical approximation of partial differential equations: Springer Berlin Heidelberg, 363–404.

Regone, C., J. Stefani, P. Wang, C. Gerea, G. Gonzalez, and M. Oristaglio, 2017, Geologic model building in SEAM Phase II — Land seismic challenges: The Leading Edge, **36**, 738–749, doi: 10.1190/tle36090738.1.

Seriani, G., and E. Priolo, 1994, Spectral element method for acoustic wave simulation in heterogeneous media: Finite Elements in Analysis and Design, **16**, 337–348, doi: 10.1016/0168-874X(94)90076-0.

Šolín, P., J. Červený, and I. Doležel, 2008, Arbitrary-level hanging nodes and automatic adaptivity in the hp-FEM: Mathematics and Computers in Simulation, **77**, 117–132, doi: 10.1016/j.matcom.2007.02.011.

Song, J.-H., P. M. A. Areias, and T. Belytschko, 2006, A method for dynamic crack and shear band propagation with phantom nodes: International Journal for Numerical Methods in Engineering, **67**, 868–893, doi: 10.1002/nme.1652.

Strouboulis, T., I. Babuška, and K. Copps, 2000, The design and analysis of the generalized finite element method: Computer Methods in Applied Mechanics and Engineering, **181**, 43–69, doi: 10.1016/S0045-7825(99)00072-9.

Strouboulis, T., I. Babuška, and R. Hidajat, 2006, The generalized finite element method for Helmholtz equation: Theory, computation, and open problems: Computer Methods in Applied Mechanics and Engineering, **195**, 4711–4731, doi: 10.1016/j.cma.2005.09.019.

Strouboulis, T., R. Hidajat, and I. Babuška, 2008, The generalized finite element method for Helmholtz equation — Part 2: Effect of choice of handbook functions, error due to absorbing boundary conditions and its assessment: Computer Methods in Applied Mechanics and Engineering, **197**, 364–380, doi: 10.1016/j.cma.2007.05.019.

Vamaraju, J., M. K. Sen, J. De Basabe, and M. Wheeler, 2018, Enriched Galerkin finite element approximation for elastic wave propagation in fractured media: Journal of Computational Physics, **372**, 726–747, doi: 10.1016/j.jcp.2018.06.049.

Vigh, D., and E. W. Starr, 2008, 3D prestack plane-wave, full-waveform inversion: Geophysics, **73**, no. 5, VE135–VE144, doi: 10.1190/1.2952623.

Virieux, J., and S. Operto, 2009, An overview of full-waveform inversion in exploration geophysics: Geophysics, **74**, no. 6, WCC1–WCC26, doi: 10.1190/1.3238367.

Wright, V., and P. Smart, 1994, Chapter 13 Paleokarst (dissolution diagenesis): Its occurrence and hydrocarbon exploration significance, Developments in sedimentology: Elsevier 51, 477–517.

Yue, B., and M. N. Guddati, 2005, Dispersion-reducing finite elements for transient acoustics: The Journal of the Acoustical Society of America, **118**, 2132–2141, doi: 10.1121/1.2011149.

Zhu, J., and L. R. Lines, 1998, Comparison of Kirchhoff and reverse-time migration methods with applications to prestack depth imaging of complex structures: Geophysics, **63**, 1166–1176, doi: 10.1190/1.1444416.

Biographies and photographs of the authors are not available.